

# Magnetic Particle Imaging Using an Optically Pumped Magnetometer Coupled With a Flux Transformer

Sasayama, Teruyoshi

Department of Electrical and Electronic Engineering, Kyushu University

Taue, Shuji

School of System Engineering, Kochi University of Technology

Yoshida, Takashi

Department of Electrical and Electronic Engineering, Kyushu University

<https://hdl.handle.net/2324/7363247>

---

出版情報 : IEEE Transactions on Instrumentation and Measurement. 74, pp.4008208-, 2025-04-21.  
Institute of Electrical and Electronics Engineers (IEEE)

バージョン :

権利関係 : © 2025 IEEE. Personal use of this material is permitted. Permission from IEEE must be obtained for all other uses, in any current or future media, including reprinting/republishing this material for advertising or promotional purposes, creating new collective works, for resale or redistribution to servers or lists, or reuse of any copyrighted component of this work in other works.





# Magnetic Particle Imaging Using an Optically Pumped Magnetometer Coupled with a Flux Transformer

Teruyoshi Sasayama, *Member, IEEE*, Shuji Taue, and Takashi Yoshida, *Member, IEEE*

**Abstract**— We propose a magnetic particle imaging (MPI) scanner using an optically pumped magnetometer (OPM) that is connected via a flux transformer. The OPM has high sensitivity, but it cannot operate in the excitation magnetic field used to magnetize the magnetic nanoparticles because of its narrow dynamic range. As a result, a flux transformer is used in this work to overcome the problem. Furthermore, the excitation current amplitude was maintained at a constant level using real-time feedback control and wavelet denoising was used to reduce the measurement noise. The results demonstrate that the position of a 100  $\mu\text{g}$ -Fe Resovist magnetic nanoparticle sample can be estimated successfully via an inverse problem analysis approach to within an error of 5 mm even when the sample is located at depths of 25–50 mm from the pickup coil.

**Index Terms**—Flux transformer, inverse problem, magnetic nanoparticle, magnetic particle imaging, optically pumped magnetometer

## I. INTRODUCTION

**B**IOSENSING using magnetic markers in the form of bio-functionalized magnetic nanoparticles (MNPs) has been studied widely for biomedical applications with examples that include detection of biological targets, target purification, hyperthermia therapy, and drug delivery [1],[2]. One particular application of magnetic markers is magnetic particle imaging (MPI), which is highly suitable for clinical applications, such as angiography, cancer imaging, and inflammation imaging, and also for research applications including stem cell imaging and small animal imaging [3]-[5].

MPI uses the nonlinearity of the magnetization curves of the MNPs in combination with the fact that the MNPs saturate a specific magnetic field strength. If an AC magnetic field with a frequency  $f_1$  and a sufficiently high amplitude is applied, the magnetic material will then exhibit a magnetization that contains not only the drive frequency  $f_1$  but also a series of harmonic frequencies. These higher frequencies can be separated from the received signal easily through appropriate

filtering. If the magnetic particles are also exposed to a DC magnetic field with a sufficiently large magnitude, the MNPs will saturate and generation of the harmonics is suppressed. Therefore, tomographic images can be generated by steering the point at which the DC magnetic field reaches zero, which is called the field-free point (FFP), when passing through the volume of interest [3],[4].

However, several problems must be resolved before an MPI scanner can be applied to the human body. First, it is difficult to generate a gradient magnetic field for FFPs (generally 1–2 T/m) that is strong enough to obtain an image [3],[4]. Second, patient safety regulations with regard to exposure to high-power and high-frequency electromagnetic fields must be also followed [6],[7].

To overcome these problems, several research groups have reported use of low-power and low-frequency MPI. Generally, the magnetic field from the MNPs is detected using a receiver coil. However, because the induced voltage is proportional to the frequency in accordance with Faraday's law, the voltage output by the receiver coil decreases at low frequencies. Therefore, high sensitivity magnetic sensors such as magnetoresistive (MR) sensors must be used [8].

In addition to MR devices, the optically pumped magnetometer (OPM) is another magnetic sensor that can measure low-frequency magnetic fields with high sensitivity (Theoretically the sensitivity limit is on the order of 0.01 fT  $\sqrt{\text{Hz}}$ ) [9],[10]. An OPM has a sensitivity that is theoretically comparable to or exceeds that of an MR sensor (The sensitivity limit is on the order of 1 pT  $\sqrt{\text{Hz}}$ ) [11] and a superconducting quantum interference device (SQUID) (The sensitivity limit is on the order of fT  $\sqrt{\text{Hz}}$ ) [12], and it is thus promising as a high-sensitivity magnetic sensor. Furthermore, an OPM does not require use of a refrigerant such as liquid helium, which would be required for a SQUID. In contrast, the disadvantage of OPM is its small dynamic range and the difficulty involved in using it directly in general MPI. Several research groups have reported MNP imaging methods using OPM that take these disadvantages into account. Colombo et al. proposed a 1D MPI

Manuscript received 19 July 2024; revised ??, August 2024; accepted September 2024. Date of publication ?? September 2024; date of current version ?? December 2024. This work was supported by the Japan Society for the Promotion of Science (JSPS) KAKENHI, Grant Numbers JP23K20939 and JP20H05652. Corresponding author: T. Sasayama (e-mail: saasayama@sc.kyushu-u.ac.jp).

T. Sasayama is with the Department of Electrical and Electronic Engineering, Kyushu University, Fukuoka 819-0395, Japan (e-mail: saasayama@sc.kyushu-u.ac.jp).

S. Taue is with the School of System Engineering, Kochi University of Technology, Kochi 782-8502, Japan.

T. Yoshida is with the Department of Electrical and Electronic Engineering, Kyushu University, Fukuoka 819-0395, Japan.

Color versions of one or more of the figures in this article are available online at <http://????????>

Digital Object Identifier ????????

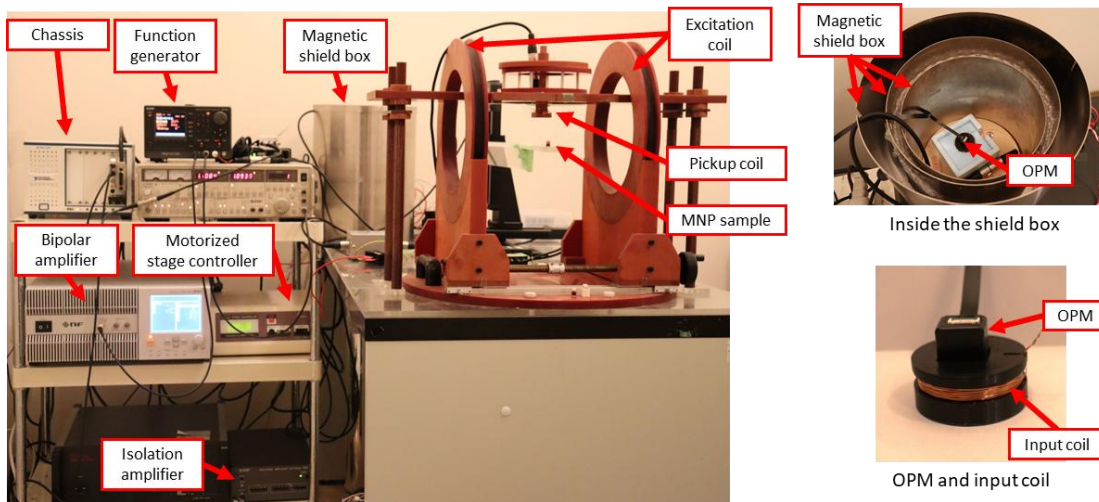
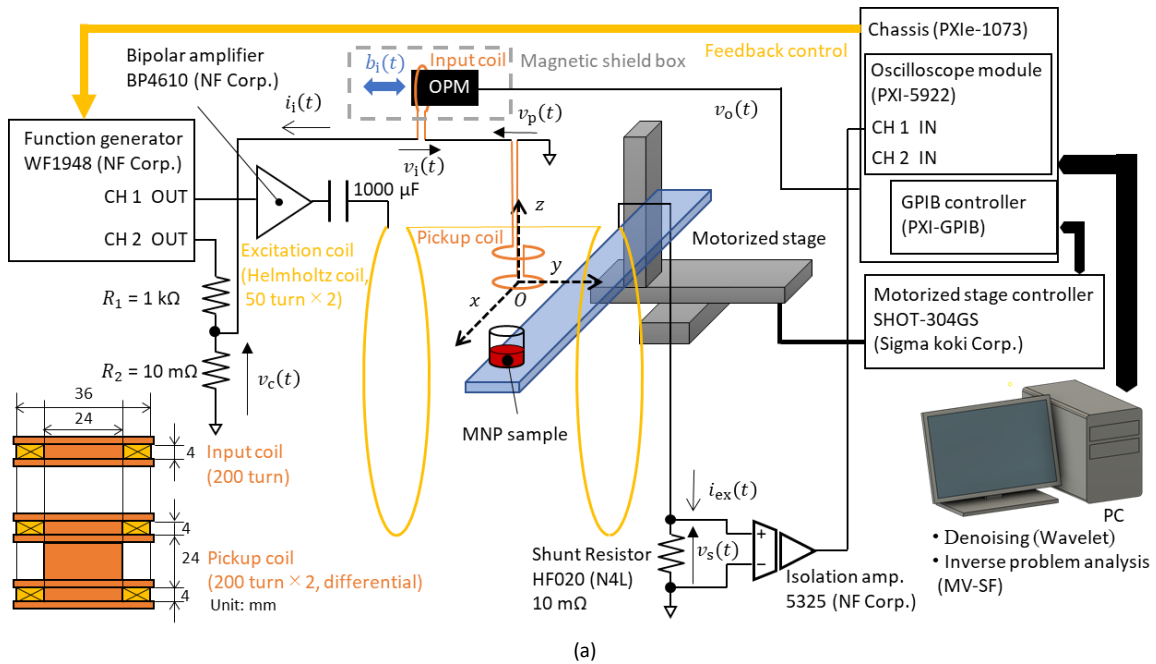


Fig. 1. Experimental setup used for OPM-MPI. (a) Schematic diagram and (b) photograph.

susceptometer (MPIS) that uses a high-sensitivity OPM to record the spatial distribution of the fluid-suspended MNPs [13]. Although this approach achieved both high spatial resolution (approximately 2.5 mm) and high sensitivity (2 pT/ $\sqrt{\text{Hz}}$ ), it also has the problem of a very narrow field of view (spanning approximately 40 mm) because of its use of coils to generate the gradient magnetic field. Jaufenthaler et al. proposed a 3D MPI method that used OPM through magnetorelaxometry imaging (MRXI) [14], [15]. MRXI uses magnetic field pulses within the mT range to acquire the MNP relaxation signal, rather than an AC magnetic field and a gradient field. Although MRXI was used successfully to reconstruct a human head sized phantom filled with immobilized MNP samples with a clinically relevant iron amount (the MNP sample size was  $12 \times 12 \times 12 \text{ mm}^3$  and the density was approximately  $3.7 \text{ mg-Fe/cm}^3 = 3.7 \text{ }\mu\text{g-Fe}/\mu\text{l}$ , i.e.,  $6.4 \text{ mg-Fe}$ ), the disadvantages of the method are that MRXI

requires a magnetically shielded room because of the small dynamic range of the OPM module and the measurement time required to image the MNP samples is also rather long (approximately 6 minutes). Therefore, OPM-MPI is desirable for 3D position estimation of MNPs with high temporal resolution and without use of a magnetically shielded room.

As a preliminary experiment, we developed an AC susceptometer with an OPM and a flux transformer [16]-[18] and detected magnetic fields from MNPs successfully without a magnetically shielded room [19]. Based on our findings from the study, we then proposed an OPM-MPI scanner that is connected via a flux transformer to operate under a low-frequency excitation magnetic field [20]. In this paper, the original method is improved by performing feedback control of the excitation current and the bridge balance to enhance the signal acquired from the MNPs. Furthermore, denoising was also performed to enhance the position estimation accuracy.

## II. MATERIALS AND METHODS

### A. Overview of Experimental Setup

Fig. 1 shows an overview of the developed OPM-MPI system.

A function generator (WF1948, NF Corp., Japan) was used to generate a sinusoidal wave. A bipolar amplifier (BP4610, NF Corp., Japan) then amplified the signal and used it to excite the Helmholtz coil, which was used in our previous MPI scanner [21]. The diameter of this Helmholtz coil was 300 mm and the distance between the two coils was 300 mm. The number of turns in each coil was set at 50. The Helmholtz coil generated a magnetic field along the  $y$ -axis. The MNP samples were magnetized using an excitation field and differential pickup coil was used to detect the magnetic field generated by the MNP samples in the  $z$ -axis direction.

The pickup coil voltage was amplified using a flux transformer that contained a pickup coil, an input coil, and an OPM (Zero-Field Magnetometer (QZFM) Gen-3, QuSpin Corp., Inc., CO, USA) that has also been used in studies by other researchers [15]. The noise level of the OPM module was less than 15 fT/ $\sqrt{\text{Hz}}$ . The excitation and pickup coils were oriented in the  $y$ - and  $z$ -axis directions, respectively, to ensure that the excitation field and the detection direction of the pickup coil were orthogonal.

The amplitude and phase of the sine wave were adjusted to be within the range measured by the OPM. The differential voltage between the voltage from the differential pickup coil ( $v_p(t)$ ) and that generated using the function generator ( $v_c(t)$ ) was amplified using a flux transformer. A shunt resistance (HF020, Newtons 4th Ltd., UK) was then used to obtain the excitation current  $i_{\text{ex}}(t)$ . Finally, the output voltage from the OPM  $v_o(t)$  and the voltage across the shunt resistance  $v_s(t)$ , were measured using an oscilloscope module with 24-bit resolution (PXI-5922, National Instruments (NI) Corp., TX, USA).

Although the amplitude of the output voltage from the bipolar amplifier remained fixed, the amplitude of  $i_{\text{ex}}(t)$  varied with the resistance changes that is occurred because of the coil temperature change caused by Joule heating. Therefore, in the previous study [20], the excitation current amplitude was set to 20 A<sub>pp</sub> (= 10 A<sub>peak</sub>) to ensure that it did not exceed the allowable output range. In this paper, the excitation current amplitude was maintained constant value via real time feedback control using LabVIEW (NI Corp.), which adjusted the amplitude of the output voltage based on the measured current amplitude. Feedback control was performed using a proportional control approach as follows:

$$V_{\text{DA1}} \leftarrow \{1 + K_P(I_{\text{target}} - I_{\text{ex}})\}V_{\text{DA1}} \quad (1)$$

where  $K_P$  is the proportional gain,  $V_{\text{DA1}}$  is the output voltage of the digital-to-analog converter (DAC, CH 1),  $I_{\text{target}}$  is the target excitation current amplitude value, and  $I_{\text{ex}}$  is the measured excitation current amplitude. The excitation current amplitude was set at 30 A<sub>pp</sub> (= 15 A<sub>peak</sub>). Under these conditions, the magnetic field intensity at the center of the Helmholtz coil was 1.8 mT<sub>peak</sub>.

Based on the known frequency characteristics [19] and to

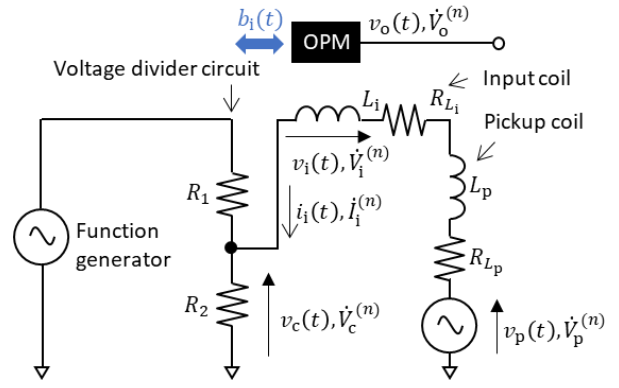


Fig. 2. Electric circuit for the flux transformer part.

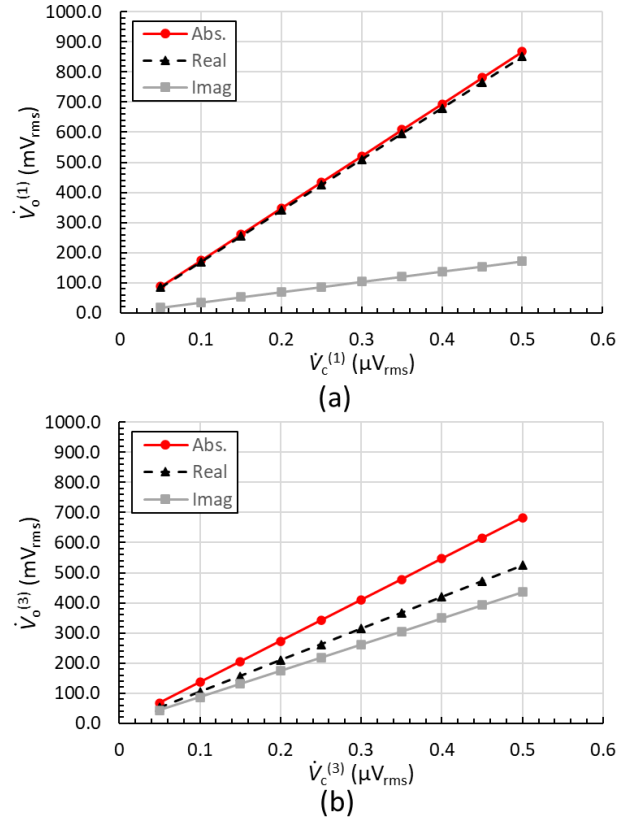


Fig. 3. Relationship between the input voltage from the bridge circuit and the output voltage from the OPM when the excitation current is zero. (a) Fundamental and (b) 3<sup>rd</sup> harmonic components.

avoid interference from the power line (fundamental frequency of 60 Hz and its harmonics (120 Hz, 180 Hz, ...)), the frequency  $f_1$  was set at 90 Hz.

### B. Flux Transformer

In accordance with our previous study [19], a flux transformer was used in the proposed setup. The OPM module can only operate under an ambient magnetic field of less than 50 nT. Therefore, the OPM module was arranged within a triple magnetic shield box composed of permalloy. The measurement with the OPM module indicated that the residual DC magnetic field including geomagnetic field was less than 50 nT (typically 30-40 nT).

The magnetic fields from the MNPs were detected using a

pickup coil. This pickup coil is a differential coil that suppresses the magnetic noise from a distance. The upper and lower coils in the pickup coil were identical, and the length, the internal diameter, the external diameter, and the number of turns of each coil were 4 mm, 24 mm, 36 mm, and 200, respectively. The distance between the two coils was 24 mm. The resistance and the inductance of the pickup coil, denoted by  $R_{L_p}$  and  $L_p$ , were 8.8  $\Omega$  and 2.8 mH, respectively.

Fig. 2 depicts the electrical circuit of the flux transformer. Ideally, the mutual inductance between the excitation and pickup coils is zero because the excitation field direction and the detection direction of the pickup coil are orthogonal. However, the magnetic flux was slightly chained because of mechanical accuracy limitations. Therefore, the fundamental component was removed using an electronic bridge circuit that comprised the output from a function generator and a voltage divider circuit ( $R_1$  and  $R_2$ ). The amplitude and the phase of the sinusoidal wave output from the function generator were adjusted to balance the bridge circuit. The dividing circuit with components  $R_1$  ( $= 1$  k $\Omega$ ) and  $R_2$  ( $= 10$  m $\Omega$ ) was then used to generate a small voltage and suppress the noise from the function generator.

The OPM was set at the center of the input coil. The length, the internal diameter, the external diameter, and the number of turns of the input coil were 4 mm, 24 mm, 36 mm, and 200, respectively. The resistance and the inductance of the pickup coil,  $R_{L_i}$  and  $L_i$ , were 4.7  $\Omega$  and 1.6 mH, respectively. The magnetic flux density at the OPM can be expressed as  $b_i(t) = ki_i(t)$ , where  $b_i(t)$  and  $i_i(t)$  represent the magnetic flux densities generated by the input coil and the input coil current, respectively. The proportionality constant  $k$  can be calculated via numerical analysis to be  $k = 8.67$  nT/ $\mu$ A.

It should be noted that the thermal noise of  $R_{L_i}$ ,  $R_{L_p}$ , and  $R_2$  affect the detection sensitivity. Therefore, thicker polyurethane enameled copper wire ( $\phi 0.315$  mm) is used for the pickup and input coils of the flux transformer to ensure low resistance, and the  $R_2$ , which is used in the voltage divider circuit, is selected to be as small as possible.

Fig. 3 illustrates the relationship between the input voltage from the bridge circuit ( $v_c(t)$ ,  $\dot{V}_c^{(n)}$ ) and the OPM output voltage ( $v_o(t)$ ,  $\dot{V}_o^{(n)}$ ) when  $\dot{V}_p^{(n)} = 0$ , where the dot above the variable ( $\dot{\quad}$ ) denotes a phasor, and the superscripted letter ( $n$ ) indicates the order of the harmonics.

In a previous study [20], the bridge balance was adjusted manually and the analog output gain of the OPM was set at 0.90 V/nT to be within the dynamic range of the oscilloscope module ( $\pm 5$  V). In this study, the bridge balance was adjusted automatically using LabVIEW, and the gain was increased to 2.70 V/nT (default value).

As Fig. 3 shows, the output voltage is proportional to the input voltage. The ratios,  $\alpha^{(1)} = -\dot{V}_o^{(1)}/\dot{V}_c^{(1)}$  and  $\alpha^{(3)} = -\dot{V}_o^{(3)}/\dot{V}_c^{(3)}$  have values of  $1.74 \times 10^6$  (V/V) and  $1.36 \times 10^6$  (V/V), respectively, where  $\alpha^{(n)}$  indicates the ratio when the frequency of  $\dot{V}_c^{(n)}$  is  $nf_1$ . As these values show,  $\alpha^{(3)}$  is slightly smaller than  $\alpha^{(1)}$ , and thus the ratios of the real and imaginary parts are

different in the fundamental and third harmonics; this corresponds to the frequency response of the OPM [17].

If  $\dot{V}_p^{(n)}$  is fixed and  $\dot{V}_c^{(n)}$  changes by  $\Delta\dot{V}_c^{(n)}$ , then the input current change  $\Delta\dot{I}_i$  can be written as

$$\Delta\dot{I}_i^{(n)} = \frac{-\Delta\dot{V}_c^{(n)} - \Delta\dot{V}_i^{(n)}}{R_{L_p} + R_{L_i} + j\omega(L_p + L_i)} \quad (2)$$

If  $\dot{V}_c$  is fixed and  $\dot{V}_p^{(n)}$  changes by  $\Delta\dot{V}_p^{(n)}$ , then  $\Delta\dot{I}_i$  can be written as

$$\Delta\dot{I}_i^{(n)} = \frac{\Delta\dot{V}_p^{(n)} - \Delta\dot{V}_i^{(n)}}{R_{L_p} + R_{L_i} + j\omega(L_p + L_i) + R_1//R_2} \quad (3)$$

where  $\omega$  denotes the angular frequency. If  $R_2 \ll |R_{L_p} + R_{L_i} + j\omega(L_p + L_i)|$ , then the relationship  $\Delta\dot{V}_c^{(n)} = -\Delta\dot{V}_p^{(n)}$  is obtained using (2) and (3). The ratio of  $\Delta\dot{V}_o^{(n)}$  to  $\Delta\dot{V}_p^{(n)}$ , which corresponds to the detection sensitivity of the MNP sample, can then be obtained as follows:

$$\frac{\Delta\dot{V}_o^{(n)}}{\Delta\dot{V}_p^{(n)}} \cong \frac{\Delta\dot{V}_o^{(n)}}{\Delta\dot{V}_c^{(n)}} \cdot \frac{\Delta\dot{V}_c^{(n)}}{\Delta\dot{V}_p^{(n)}} = -\alpha^{(n)} \cdot (-1) = \alpha^{(n)} \quad (4)$$

Here, the signal attenuation by the flux transformer is evaluated. Assuming that a magnetic flux of 1 nT, 90 Hz is chained to the pickup coil, we obtain  $|\dot{V}_p^{(1)}| = 79.9$  nV from Faraday's law of electromagnetic induction. Using the value of  $\alpha^{(1)}$ , we obtain  $|\dot{V}_o^{(1)}| = 0.139$  V. Considering that the sensitivity of the OPM is 2.70 nT/V, OPM detects 0.376 nT. This indicates that the attenuation rate of the signal is only approximately 1/3 even through the flux transformer. Note that there remains the possibility to improve the attenuation rate by optimizing the flux transformer, e.g., the input coil is wound more closely to the OPM.

### C. Point Spread Function

Resovist (Fujifilm RI Pharma, Japan) was used to form the MNP samples. The Resovist was poured into a cylindrical cell to realize the desired Fe concentration and was then diluted with glycerol to obtain 150  $\mu$ L. Two MNP sample concentrations were prepared: 100  $\mu$ g-Fe (0.66  $\mu$ g-Fe/ $\mu$ L) and 500  $\mu$ g-Fe (3.33  $\mu$ g-Fe/ $\mu$ L). Each MNP sample type was prepared in a cylindrical container ( $\phi 6$  mm  $\times$  5 mm). Each MNP sample was moved at 5 mm/s using a motorized stage (SGSP26-200 and SGSP26-150, Sigma Koki) that was controlled by a motorized stage controller (SHOT-304GS, Sigma Koki). The third harmonic of  $v_o(t)$  was obtained using a fast Fourier transform, and a point spread function was then obtained. The sampling resolution on the  $xy$  plane was set at 5 mm  $\times$  5 mm. The distance between the MNP sample and the pickup coil was set at various values within the range from 25–50 mm at intervals of 5 mm, i.e.,  $z$  was set to be within the range from  $-25$  to  $-50$  mm.

### D. Position Estimation of Magnetic Nanoparticle

The harmonic voltage vector  $\mathbf{v}$ , is expressed as [3], [21]

$$\mathbf{v} = \mathbf{A}\mathbf{c} \quad (5)$$

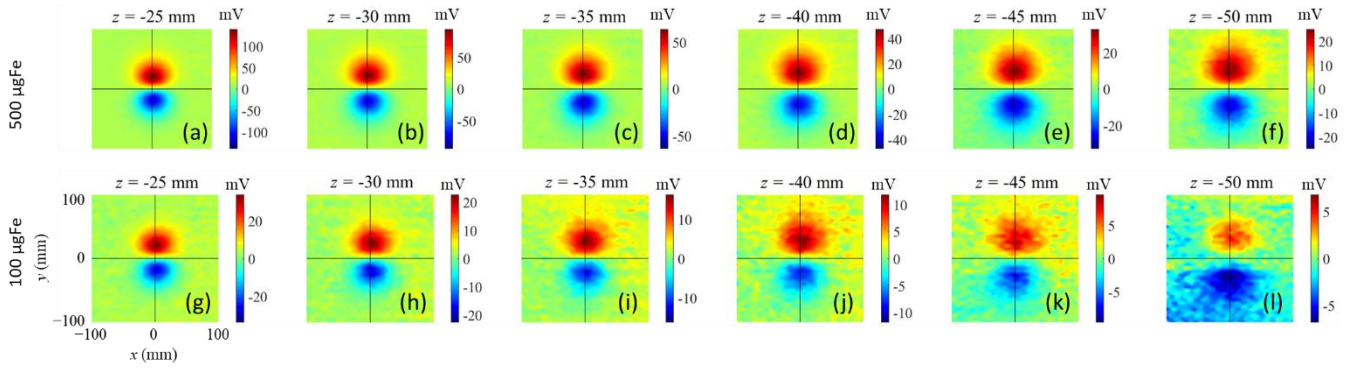


Fig. 4. Field maps of the imaginary part of the third harmonic component when (a)-(f) the 500  $\mu\text{g-Fe}$  sample and (g)-(l) the 100  $\mu\text{g-Fe}$  sample are located. The parameter  $z$  has values of (a), (g)  $-25$ , (b), (h)  $-30$ , (c), (i)  $-35$ , (d), (j)  $-40$ , (e), (k)  $-45$ , and (f), (l)  $-50$  mm.

where  $\mathbf{v}$  denotes the third-harmonic voltage vector,  $\mathbf{A}$  represents the system matrix, and  $\mathbf{c}$  represents the concentration vector, with components that are determined using the concentration at position  $\mathbf{r}$ . The expression in (5) is often described as a forward problem. The system matrix  $\mathbf{A}$  can be generated using a point spread function.

Several methods can be used to solve (5), which is an inverse problem. In accordance with the approach used in previous studies, a minimum variance spatial filter (MV-SF) [22], [23] was applied. The power of the spatial filter output  $P(\mathbf{r})$ , which corresponds to the concentration map  $\mathbf{c}$ , is estimated using the MV-SF with array gain constraint as follows:

$$\hat{P}(\mathbf{r}) = \mathbf{w}^T(\mathbf{r})\mathbf{C}\mathbf{w}(\mathbf{r}) \quad (6)$$

$$\text{subject to } \mathbf{w}(\mathbf{r})^T \mathbf{a}(\mathbf{r}) = \|\mathbf{a}(\mathbf{r})\| \quad (7)$$

where the hat ( $\hat{\cdot}$ ) indicates estimated quantities,  $\mathbf{C}$  represents the covariance matrix of  $\mathbf{v}(t)$ , and  $\mathbf{a}(\mathbf{r})$  represents the column vector of  $\mathbf{A}$ . Tikhonov regularization is then used to calculate  $\mathbf{C}^{-1}$  as  $(\mathbf{C} + \lambda \mathbf{I})^{-1}$ , where  $\mathbf{I}$  represents a unit matrix and  $\lambda$  represents a regularization parameter.

The system matrix  $\mathbf{A}$  can be obtained either numerically or experimentally. In this study, the system matrix  $\mathbf{A}$  was generated using the point spread function that was obtained by scanning the 500  $\mu\text{g-Fe}$  sample.

### E. Denoising

The system matrix  $\mathbf{A}$  contains noise in its measured values caused by the thermal noise from the flux transformer and other noise sources, e.g., external magnetic noise. To reduce this noise, a built-in function in MATLAB R2024a (Mathworks, Inc., MA, USA), `wdenoise2`, which denoises images using wavelets [24], was applied.

## III. RESULTS AND DISCUSSION

### A. Point Spread Function

Fig. 4 show the results for the point spread function, i.e., these figures present the field maps of the imaginary part of the third harmonic component when the 500 and 100  $\mu\text{g-Fe}$  samples are located, respectively. The amplitude of the signal in Fig. 4 is approximately 5 times stronger than that in the previous study [19] due to the improvement of excitation

current and the analog output gain of the OPM module (from

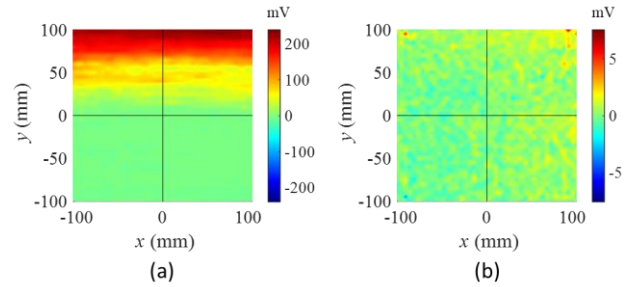


Fig. 5. Field maps of the imaginary part of the third harmonic component measured when no sample is present, (a) without feedback control and (b) with feedback control.

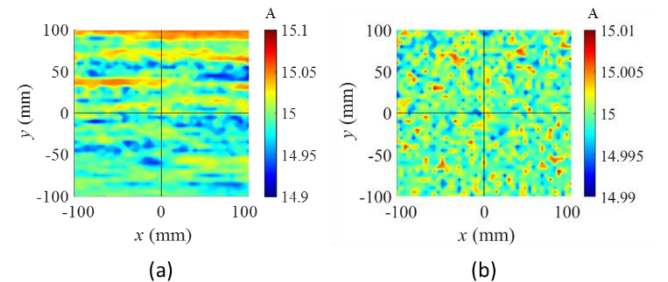


Fig. 6. Excitation current maps measured when no sample is present, (a) without feedback control and (b) with feedback control.

20  $A_{pp}$  to 30  $A_{pp}$  and from 0.90 V/nT to 2.70 V/nT, respectively) by the feedback control.

As depicted in Fig. 4(a)-(f), the signal is maximal for positive  $y$  values, whereas the signal becomes minimal for negative  $y$  values. This behavior occurs because the magnetization direction is the  $y$ -axis direction. The signal becomes weaker and the distribution broadens as the distance between the pickup coil and the MNP sample increases.

Comparison of Fig. 4(a)-(f) and Fig. 4(g)-(l) shows that the signal is greater in the more dense case (Fig. 4(a)-(f)) than in the less dense case (Fig. 4(g)-(l)). Nevertheless, the signal from the MNPs was observed under all conditions. Even in the case where the 100  $\mu\text{g-Fe}$  sample was located at  $z = -50$  mm, the peak value still exceeded 4.00  $mV_{peak}$ .

### B. Performance of the Feedback Control Method and Noise Level

To evaluate the performance of the feedback control approach for the excitation current and the noise level signal, field maps

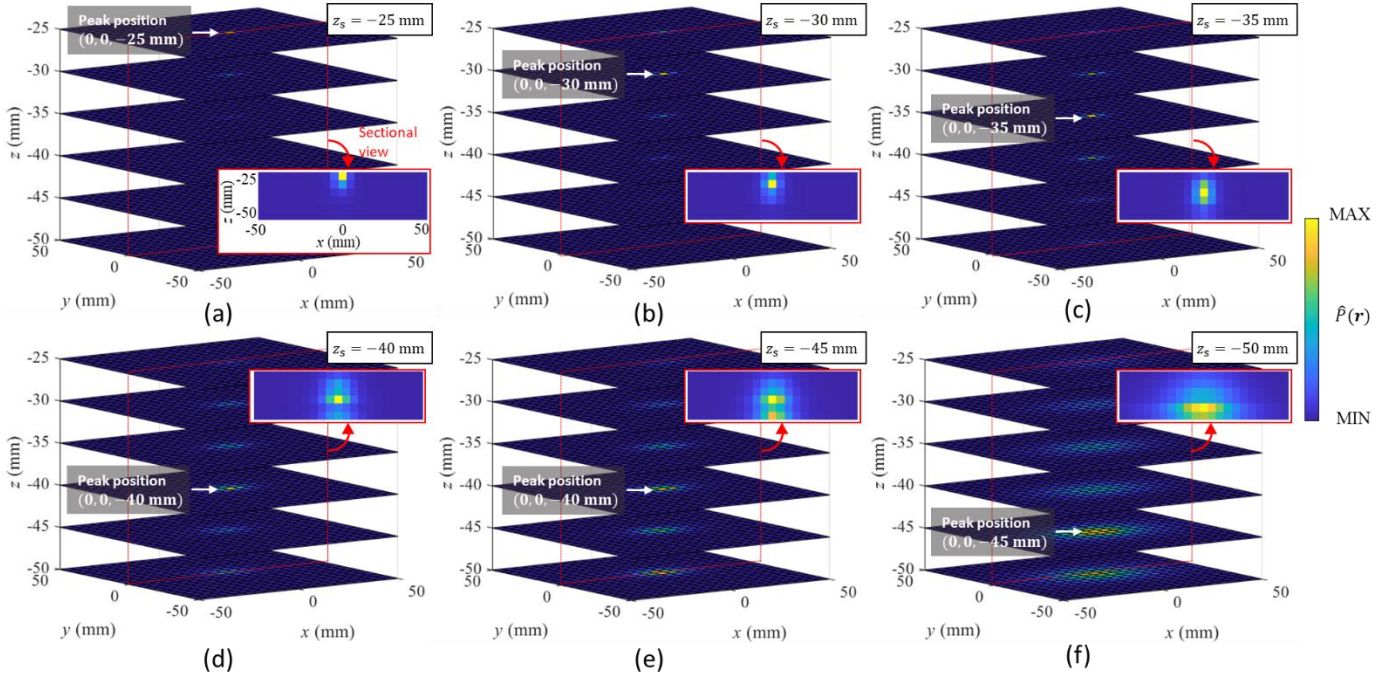


Fig. 7. Maps reconstructed using the MV-SF method when the 100  $\mu\text{g}$ -Fe MNP sample is located. The actual MNP sample positions are given by  $x_s = 0$  mm,  $y_s = 0$  mm, and  $z_s$  values of (a) -25, (b) -30, (c) -35, (d) -40, (e) -45, and (f) -50 mm.

of the imaginary part of the third harmonic component were also measured when no sample was present. Figs. 5 and 6 show the field maps of the imaginary part of the third harmonic component and the corresponding excitation current maps, respectively, when no sample is located without and with feedback control. As shown in Fig. 6(a), the maximum excitation current error is approximately 100 mA without feedback control. In contrast, as shown in Fig. 6(b), the maximum excitation coil current error is less than 10 mA with feedback control. Comparison of Fig. 5 and Fig. 6 shows that the significant changes observed in the excitation current also affect the field maps of the third harmonic. Furthermore, because the variation in the excitation current also affects the variation in the fundamental wave, it was necessary to reduce the analog output gain of the OPM module from the previous study (0.90 V/nT) [19] to ensure that it would not exceed the measurement range of the OPM module without use of feedback control. Therefore, feedback control of the excitation current is effective when used in high-sensitivity measurements.

The standard deviation (SD) of the noise shown in Fig. 5(b) is 0.770 mV<sub>peak</sub>. The peak value exceeds 3SD (which is statistically significant); therefore, it was concluded that the magnetic signal from the 100  $\mu\text{g}$ -Fe sample when located at  $z = -50$  mm can be detected using the OPM-MPI scanner.

According to the nominal values given by manufacturer, the OPM module's noise level is less than 15 fT/ $\sqrt{\text{Hz}}$ . In this study, the analog output gain of the OPM was set at 2.70 V/nT. Therefore, the output noise from the OPM corresponds to a value of 40.5  $\mu\text{V}/\sqrt{\text{Hz}}$ . Considering the value of  $\alpha^{(1)}$ , the input voltage noise is 10 pV/ $\sqrt{\text{Hz}}$ , which is two orders of magnitude less than the input voltage noise of a low-noise amplifier

(typically 1 nV/ $\sqrt{\text{Hz}}$ ). In contrast, the output noise from the OPM caused by  $R_{Lp}$ ,  $R_{Li}$ ,  $R_1$ , and  $R_2$  can be estimated to be

$$\alpha^{(3)}\sqrt{4k_BTR_{\text{total}}} \quad (8)$$

where  $k_B$  is Boltzmann's constant ( $1.38 \times 10^{-23}$  J/K),  $T$  is the absolute temperature of the resistance, and  $R_{\text{total}} = R_{Lp} + R_{Li} + R_1 // R_2 = 13.5 \Omega$ . If we assume that  $T = 300$  K, then the output noise becomes 0.643 mV/ $\sqrt{\text{Hz}}$ . Therefore, the noise observed in Fig. 6(b) is primarily caused by the thermal noise of the flux transformer. In future work, we intend to reduce the resistance values of the pickup and input coils by tuning the sizes of these coils, using thicker coil wire, and cooling the coils [17].

#### C. Inverse Problem

Fig. 7 shows the maps that were reconstructed using (6) when the 100  $\mu\text{g}$ -Fe MNP sample was located at  $(x_s, y_s, z_s)$ , where  $x_s = 0$  mm,  $y_s = 0$  mm, and  $z_s = -25, -30, \dots, -50$  mm. The results obtained indicate that the distance between the signal peak position and the actual sample position, i.e., the estimation error, is less than or equal to 5 mm, even though the estimated signal strength distribution broadens as  $z_s$  decreases, and the estimation performance is considered to be sufficiently accurate.

#### D. Point Spread Function after Denoising

Fig. 8 show the results obtained for the point spread function, i.e., the field maps of the imaginary part of the third harmonic component when the 500 and 100  $\mu\text{g}$ -Fe samples are located, respectively. When compared with the results shown in Fig. 4, the noise has effectively been eliminated, particularly in the cases where the signal becomes weaker as the depth increases.

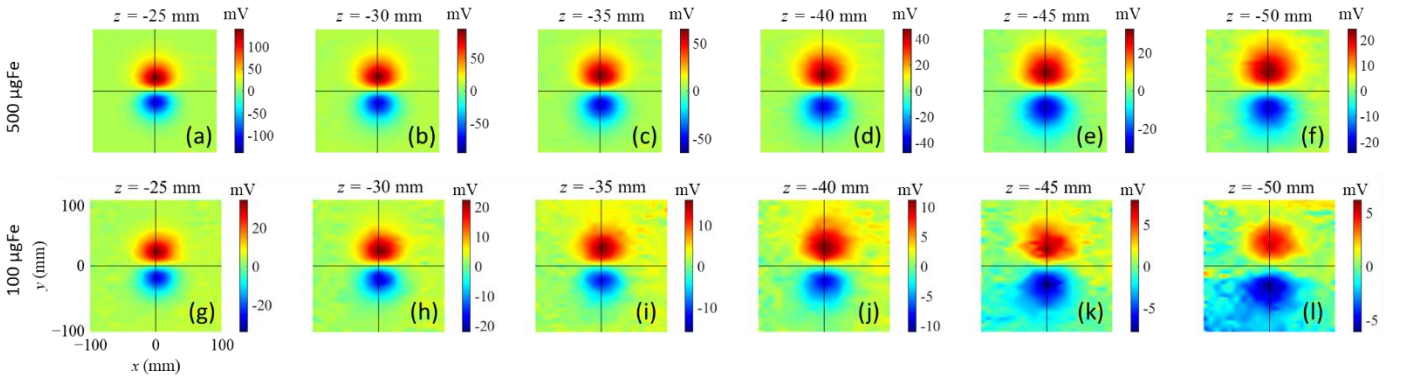


Fig. 8. Field maps of the imaginary part of the third harmonic component after denoising when (a)-(f) the 500  $\mu\text{g-Fe}$  sample and (g)-(l) the 100  $\mu\text{g-Fe}$  sample are located. The parameter  $z$  has values of (a), (g)  $-25$ , (b), (h)  $-30$ , (c), (i)  $-35$ , (d), (j)  $-40$ , (e), (k)  $-45$ , and (f), (l)  $-50$  mm.

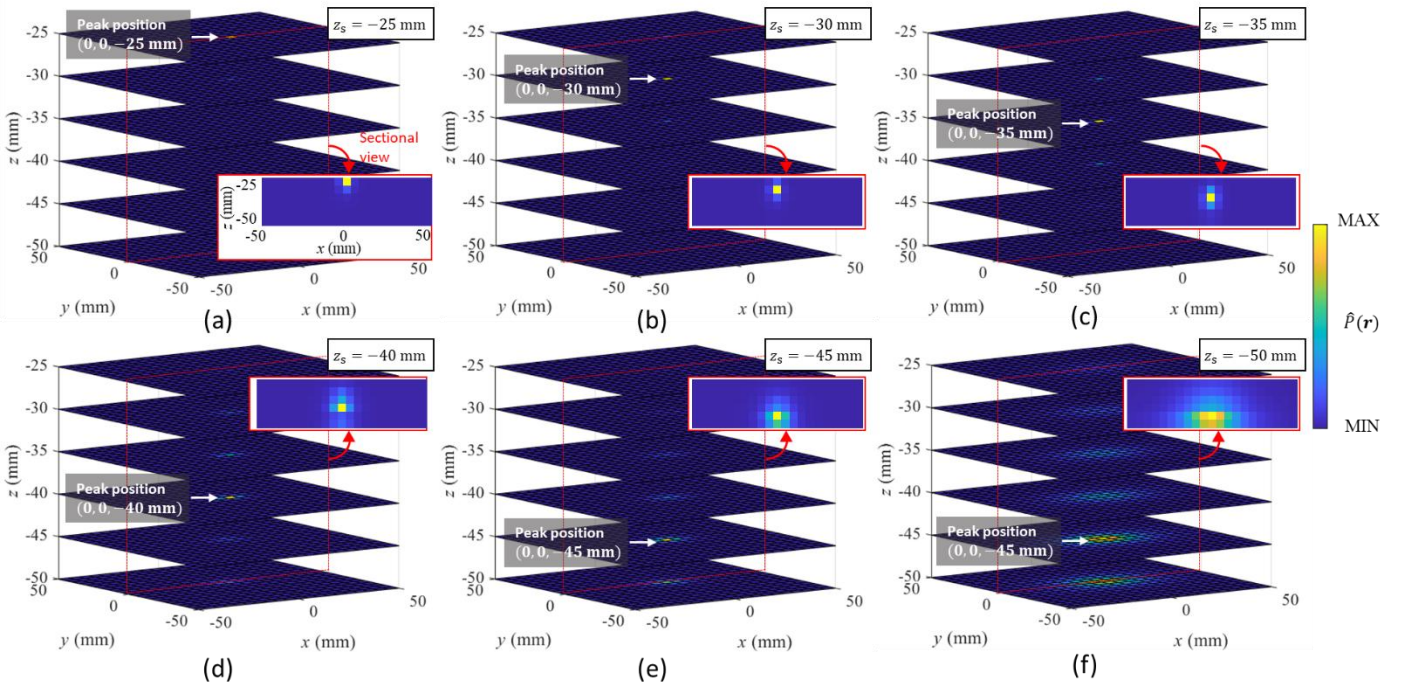


Fig. 9. Maps reconstructed using the MV-SF method when the 100  $\mu\text{g-Fe}$  MNP sample is located after denoising. The actual MNP sample positions are given by  $x_s = 0$  mm,  $y_s = 0$  mm, and  $z_s$  values of (a)  $-25$ , (b)  $-30$ , (c)  $-35$ , (d)  $-40$ , (e)  $-45$ , and (f)  $-50$  mm.

### E. Inverse Problem using Denoised Data

Fig. 9 shows the maps that were reconstructed using (6) when the 100  $\mu\text{g-Fe}$  MNP sample was located at  $(x_s, y_s, z_s)$ , where  $x_s = 0$  mm,  $y_s = 0$  mm, and  $z_s = -25, -30, \dots, -50$  mm after denoising. When compared with the results shown in Fig. 7, the estimated signal spread is narrower. Moreover, the position estimation error decreases over the range from 5 mm to 0 mm at  $z_s = -45$  mm. The results above indicate that denoising of the system matrix improves the position estimation accuracy.

In contrast, the position estimation error recorded at  $z_s = -50$  mm is still 5 mm, even after denoising. To improve the accuracy in this case, we intend to optimize the specifications of the excitation, pickup, and input coils to enhance the magnetic signal obtained from the MNPs. Furthermore, we also intend to reduce the noise of the point spread function. In addition to examination of other image denoising methods as alternatives to wavelet analysis, we will also examine the magnetic field

distributions of the MNPs by using experimental values for the magnetic susceptibility of the MNPs and a system matrix obtained from electromagnetic field analysis simulations [25].

### IV. CONCLUSION

In this study, we developed an MPI scanner using an OPM connected via a flux transformer in a low-frequency excitation magnetic field. The excitation current amplitude was maintained at a constant value using real time feedback control, which contributed to the scanner's increased sensitivity. The magnetic signal from a 100  $\mu\text{g-Fe}$  Resovist MNP sample was detected successfully even when the MNP sample was located at depths of 25–50 mm from the pickup coil at an excitation frequency of 90 Hz.

A 500  $\mu\text{g-Fe}$  Resovist MNP sample was scanned to obtain the system matrix. The 100  $\mu\text{g-Fe}$  Resovist MNP sample's position was estimated via inverse problem analysis. Consequently, the sample position was estimated to within an error of 5 mm.

Furthermore, we also demonstrated that wavelet denoising improved the estimation accuracy.

In this study, only one axis component in a single OPM module was used. In the future, we will construct a more sensitive and accurate multi-channel MPI while considering the effects of crosstalk noise.

#### ACKNOWLEDGMENT

We thank David MacDonald, MSc, from Edanz (<https://jp.edanz.com/ac>) for editing a draft of this manuscript.

#### REFERENCES

- [1] Q. A. Pankhurst, J. Connolly, S. K. Jones, and J. Dobson, "Applications of magnetic nanoparticles in biomedicine," *J. Phys. D: Appl. Phys.*, vol. 36, pp. R167–R181, 2003.
- [2] K. Enpuku, Y. Tsujita, K. Nakamura, T. Sasayama, and T. Yoshida, "Biosensing utilizing magnetic markers and superconducting quantum interference devices," *Supercond. Sci. Technol.*, vol. 30, 2017, Art. no. 053002.
- [3] B. Gleich and J. Weizenecker, "Tomographic imaging using the nonlinear response of magnetic particles," *Nature*, vol. 435, no. 7046, pp. 1214–1217, 2005.
- [4] T. Knopp and T. M. Buzug, *Magnetic Particle Imaging—An Introduction to Imaging Principles and Scanner Instrumentation*. Berlin, Germany: Springer-Verlag 2012.
- [5] A. Neumann, K. Grafé, A. von Gladiss, et al., "Recent developments in magnetic particle imaging," *J. Magn. Magn. Matter.*, vol. 550, 2022, Art. no. 169037.
- [6] O. Dössel and J. Bohnert, "Safety considerations for magnetic fields of 10 mT to 100 mT amplitude in the frequency range of 10 kHz to 100 kHz for magnetic particle imaging," *Biomed. Eng.*, vol. 58, no. 6, pp. 611–621, 2013.
- [7] O. B. Demirel and E. U. Saritas, "Effects of duty cycle on magnetostimulation thresholds in MPI," *Int. J. Magn. Part. Imag.*, vol. 3, no. 1, 2017, Art. no. 703010.
- [8] S. B. Trisnanto, T. Kasajima, T. Akushichi, and Y. Takemura, "Sub-pT oscillatory magnetometric system using magnetoresistive sensor array for a low-field magnetic particle imaging," *AIP Adv.*, vol. 13, no. 2, 2023, Art. no. 025113.
- [9] I. K. Kominis, T. W. Kornack, J. C. Allred, and M. V. Romalis, "A subfemtotesla multichannel atomic magnetometer," *Nature*, vol. 422, no. 6932, pp. 596–599, Apr. 2003.
- [10] H. Xia, A. Ben-Amar Baranga, D. Hoffman, and M. V. Romalis, "Magnetoencephalography with an atomic magnetometer," *Appl. Phys. Lett.*, vol. 89, no. 21, 2006, Art. no. 211104.
- [11] N. A. Stutzke, S. E. Russek, D. P. Pappas, and M. Tondra, "Low-frequency noise measurements on commercial magnetoresistive magnetic field sensors," *J. Appl. Phys.*, vol. 97, no. 10, 2005, Art. no. 10Q107.
- [12] J. Gallop, "SQUIDS: some limits to measurement," *Supercond. Sci. Technol.*, vol. 16, no. 12, pp. 1575–1582, 2003.
- [13] S. Colombo, V. Lebedev, A. Tonyushkin, S. Pengue, and A. Weis, "Imaging magnetic nanoparticle distributions by atomic magnetometry-based susceptometry" *IEEE Trans. Med. Imag.*, vol. 39, no. 4, pp. 922–933, 2020.
- [14] J. Aaron, S. Peter, M. Thomas, L. Maik, W. Frank, and B. Daniel, "Quantitative 2D magnetorelaxometry imaging of magnetic nanoparticles using optically pumped magnetometers," *Sensors*, vol. 20, no. 3, 2020, Art. no. 753.
- [15] A. Jaufenthaler, T. Sander, P. Schier, K. Pansegrau, F. Wiekhorst, and D. Baumgarten, "Human head sized magnetorelaxometry imaging of magnetic nanoparticles with optically pumped magnetometers—a feasibility study," *J. Magn. Magn. Matter.*, vol. 596, 2024, Art. no. 171983.
- [16] F. Baudenbacher, N. T. Peters, and J. P. Wikswo, Jr., "High resolution low-temperature superconductivity superconducting quantum interference device microscope for imaging magnetic fields of samples at room temperatures," *Rev. Sci. Instrum.*, vol. 73, no. 3, pp. 1247–1254 2002.

- [17] Q. Yang, K. Yao, D. Yamasaki, and K. Enpuku, "Magnetometer utilizing cooled normal pickup coil and high-Tc superconducting quantum interference device picovoltmeter for nondestructive evaluation," *Jpn. J. Appl. Phys.*, vol. 44, no. 20, pp. L626–L628, 2005.
- [18] T. Oida, Y. Kawamura, and T. Kobayashi, "Optimization of flux transformer for optically pumped atomic magnetometer in ultra-low field MRI systems," *IEEE Trans. Magn.*, vol. 47, no. 10, pp. 3074–3077, 2011.
- [19] T. Sasayama, S. Taue, and T. Yoshida, "AC susceptibility measurement of magnetic nanoparticles using an optically pumped magnetometer and a flux transformer," *AIP Adv.*, vol. 14, no. 1, 2024, Art. no. 015029.
- [20] T. Sasayama, S. Taue, and T. Yoshida, "Magnetic particle imaging using an optically pumped magnetometer and a flux transformer," in *Proc. FMTC*, Glasgow, United Kingdom, May 20–23, 2024.
- [21] T. Sasayama, Y. Tsujita, M. Morishita, M. Muta, and K. Enpuku, "Three-dimensional magnetic nanoparticle imaging using small field gradient and multiple pickup coils," *J. Magn. Magn. Mater.*, vol. 427, pp. 143–149, 2017.
- [22] K. Sekihara and S. S. Nagarajan, "Adaptive Spatial Filters for Electromagnetic Brain Imaging," New York, NY, USA: Springer-Verlag, 2008.
- [23] N. Okamura, T. Sasayama, and K. Enpuku, "Inverse Problem Analysis in Magnetic Nanoparticle Tomography Using Minimum Variance Spatial Filter," *IEEE Trans. Magn.*, Vol. 58, No. 2, 2022, Art. no. 6500305.
- [24] Mathworks Inc. *Wavelet image denoising - MATLAB wdenoise2 - MathWorks*. Accessed: July 18, 2024. [Online]. Available: <https://www.mathworks.com/help/wavelet/ref/wdenoise2.html>
- [25] N. Futagawa, M. Fujimoto, K. Higashino, T. Sasayama, and T. Yoshida, "Imaging of Magnetic Nanoparticles Using AC Susceptibility Data," *IEEE Trans. Magn.*, vol. 59, no. 11, 2023, Art. no. 5101205.



**Teruyoshi Sasayama** (Member, IEEE) received his B. Eng., M. Eng., and Dr. Eng. degrees from Kyoto University, Kyoto, Japan, in 2007, 2009, and 2012, respectively. He is an associate professor in the Faculty of Information Science and Electrical Engineering, Kyushu University. His research interests include in biomedical applications of magnetic nanoparticles and electromagnetic nondestructive testing.



**Shuji Taue** received his B. Eng., M. Eng., and Dr. Eng. degrees from Tokushima University, Tokushima, Japan, in 2000, 2002, and 2005, respectively. He is an associate professor in the School of System Engineering, Kochi University of Technology. He has been engaged in research into optical fiber sensors and optically pumped magnetometers.



**Takashi Yoshida** (Member, IEEE) received his B. Eng., M. Eng., and Dr. Eng. degrees from Kyushu University, Fukuoka, Japan, in 1998, 2000, and 2003, respectively. He is a professor in the Faculty of Information Science and Electrical Engineering, Kyushu University. He has been engaged in research into the biomedical applications of magnetic nanoparticles. His current research interest is in the development of a magnetic particle imaging system.